Unified Solution of Various Dielectric-Loaded Ridge Waveguides with a Mixed Spectral-Domain Method

KWONG T. NG, MEMBER, IEEE, AND CHI HOU CHAN, MEMBER, IEEE

Abstract—**A mixed spectral-domain method is developed and applied to analyze various dielectric-loaded ridge waveguides. Magnetic surface currents at apertures are identified as unknowns in auxiliary structures. Spectral Green's functions are formulated with the spectral immittance approach for these structures. Mixing different spectral domains existing on the two sides of an aperture in a spectral Galerkin approach then leads to the characteristic equations required for the dispersion analysis. The simplicity and numerical efficiency of the conventional spectral-domain immittance approach, which cannot be applied directly to the present structures, are maintained. Representative results are obtained to illustrate the application of the method.**

I. INTRODUCTION

CONVENTIONAL ridge waveguide and its variations, e.g., antipodal ridge waveguide [2] and T-septum waveguide [3], have found many applications in microwave and millimeter-wave devices [1]–[6]. The ridges in rectangular waveguides increase the cutoff wavelength and allow wave propagation with smaller overall guide dimensions than those required in rectangular waveguides. In addition, ridge waveguides offer the advantages of large bandwidths, low characteristic impedances, and the possibility of integrated circuit designs [4].

Since the original ridge waveguide structure was proposed, different variations have been made to increase its bandwidth, e.g., antipodal ridge waveguide [2] and T-septum waveguide [3]. Also, dielectric loading has been used to control its propagation characteristics [7]. In this paper a mixed spectral-domain technique will be developed for the analysis of the class of dielectric-loaded ridge waveguides shown in Fig. 1, including the dielectric-loaded antipodal and T-septum waveguides shown in Fig. 1(d) and (e). Only the symmetrical double T-septum waveguide is considered, although the method can be applied to other general T-septum waveguides with inhomogeneous dielectric slabs as well. These structures have been analyzed separately before with analytical approximations, mode-matching techniques, variational techniques, Ritz–Galerkin techniques, and the method of moments [7]–[12]. (To the best of our knowledge, the antipodal ridge waveguide has been analyzed before only without dielectric loading.) Compared to these previous methods, the technique developed in this paper is more versatile or numerically efficient.

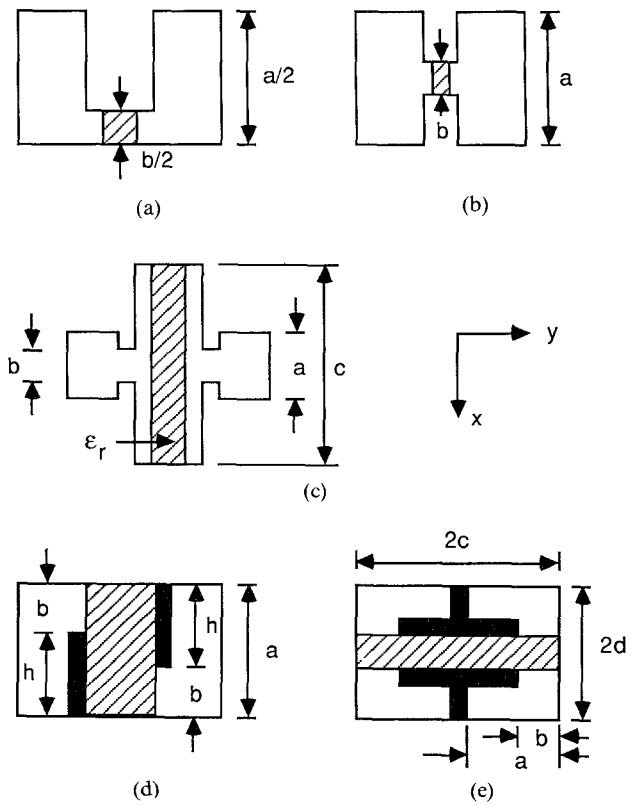

Fig. 1. A class of ridge waveguides. (a) Dielectric-loaded single-ridge waveguide. (b) Dielectric-loaded double-ridge waveguide. (c) Slotted dielectric-loaded ridge waveguide (d) Dielectric-loaded antipodal ridge waveguide. (e) Dielectric-loaded T-septum waveguide.

The spectral-domain method, using a generalized immittance approach [13], is popular for the analysis of planar and quasi-planar structures. It offers simple formulation and high numerical efficiency. With a proper choice of basis functions, only a small number of them is required, leading to a small matrix size. The conventional spectral-domain immittance approach, however, cannot be applied directly to analyze the structures shown in Fig. 1. This is

Manuscript received March 31, 1989; revised July 21, 1989.

K. T. Ng is with the Department of Electrical Engineering, University of Virginia, Charlottesville, VA 22901.

C. H. Chan was with the Department of Electrical and Computer Engineering, University of Illinois, Urbana, IL 61801. He is now with the Department of Electrical Engineering, University of Washington, Seattle, WA 98195.

IEEE Log Number 8931090

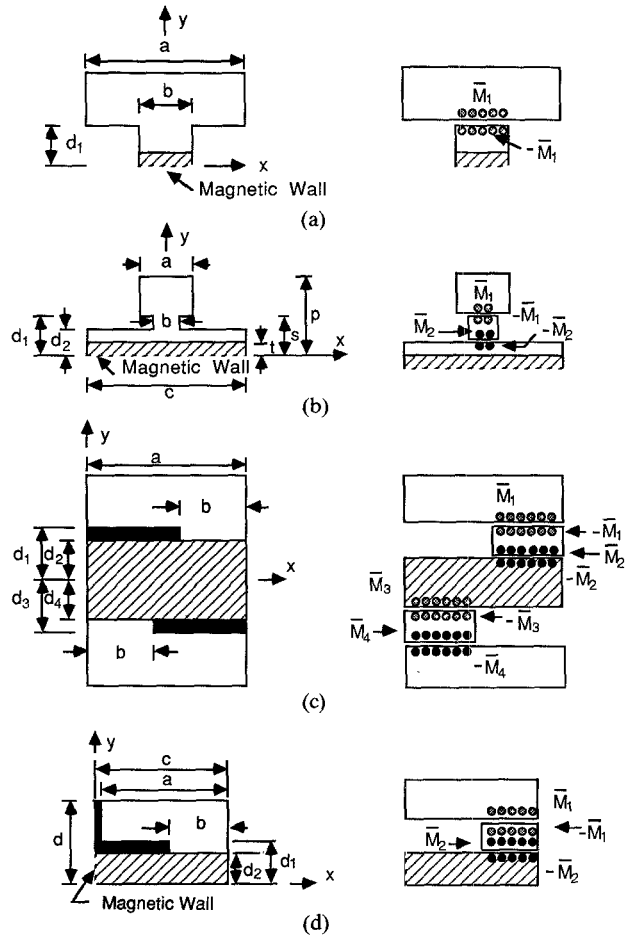

Fig. 2. Simplified structures after applying symmetry (shown on the left) and equivalent structures based on the equivalence principle (shown on the right) for the ridge waveguides shown in Fig. 1. (a) Dielectric-loaded single-ridge and double-ridge waveguide. (b) Slotted dielectric-loaded ridge waveguide. (c) Dielectric-loaded antipodal ridge waveguide. (d) Dielectric-loaded T-septum waveguide.

because the Fourier transform variable α in x will have different values for different regions, in order to satisfy the boundary conditions on the sidewalls, which have different separations in different regions. As a result, a mixed domain approach is developed, one which maintains the advantages of the spectral-domain immittance method. In the present approach, magnetic surface currents at apertures are identified as the unknowns in equivalent structures. A spectral Galerkin method involving different spectral domains is then developed, using the immittance approach to formulate Green's functions for these equivalent structures. The method is general and can be formulated to analyze other quasi-planar transmission line structures consisting of variations in sidewall separations, e.g., finlines with pedestals or grooves [14].

II. Formulation

A. Mixed Spectral-Domain Method

Because of the symmetry existing in the dielectric-loaded single-ridge and double-ridge waveguides (Fig. 1(a) and (b)), only half of each original structure need be considered, and both of them can be reduced to a structure with an electric or magnetic wall inserted at the center. Only the magnetic wall case will be considered here, as shown in Fig. 2(a), with the understanding that all the procedures are similar for the electric wall case. Similar symmetry in other ridge waveguides allows them to be reduced accordingly, as shown in Fig. 2 with their corresponding equivalent structures. Note that for the double T-septum waveguide, only one quarter of the structure need be analyzed and only modes satisfying the boundary conditions of a magnetic wall at $x = 0$ and an electric wall at $y = 0$ will be considered. Again, it should be understood that all other modes can be handled by similar procedures.

To illustrate the formulation, the slotted, dielectric-loaded ridge waveguide in Fig. 1(c) will be considered first. The spectral-domain immittance approach can then be used for the equivalent structures shown in Fig. 2(b). Following the equivalence principle [15], the two apertures in the ridge waveguide are replaced by perfectly conducting planes, and appropriate magnetic surface currents are used to restore the fields. The total transverse (to y) magnetic field at $y = d_1^+$ is radiated by magnetic surface current $\boldsymbol{M}_1$ in the presence of the conducting plane and the environment for $y > d_1$. On the other hand, the transverse magnetic fields at $y = d_1^-$ and $y = d_2^+$ are radiated by magnetic surface currents $-\boldsymbol{M}_1$ and $\boldsymbol{M}_2$ in the presence of the shorted apertures. Finally, the magnetic field at $y = d_2^-$ is due to $-\boldsymbol{M}_2$ radiating in the presence of the conducting plane and the environment for $y < d_2$. One can use the conventional spectral-domain immittance approach to easily derive the spectral dyadic Green's functions for the equivalent structures. Enforcement of continuity of the transverse magnetic fields across the apertures allows one to relate $\boldsymbol{M}_1$ and $\boldsymbol{M}_2$.

In the following, the spectral dyadic Green's functions and transverse magnetic fields will be given. Quantities marked with a tilde are Fourier transforms of corresponding quantities without the tilde. The Fourier transform is defined as in [16]. The discrete transform variables are $p\pi/a$, $p\pi/b$, and $p\pi/c$ over the regions $y > d_1$, $d_2 < y < d_1$, and $y < d_2$, respectively. Three kinds of spectral dyadic Green's functions, as illustrated in Fig. 3, are required. Their detailed expressions are given in the Appendix. In using these Green's functions, the variables d and l in Fig. 3 need to be set at values appropriate for the slotted, dielectric-loaded ridge waveguide shown in Fig. 2(b), as given in the following field expressions. The transverse magnetic fields at $y = d_1^+$ due to $\boldsymbol{M}_1$, with a shorted aperture, is

$$\begin{bmatrix} \tilde{H}_x \\ \tilde{H}_z \end{bmatrix}_{d_1^+} = \begin{bmatrix} \tilde{G}^1_{xx} & \tilde{G}^1_{xz} \\ \tilde{G}^1_{zx} & \tilde{G}^1_{zz} \end{bmatrix} \begin{bmatrix} \tilde{M}_{1x} \\ \tilde{M}_{1z} \end{bmatrix}, \qquad d = p - s. \quad (1)$$

On the other hand, the magnetic fields at $y = d_1^-$ due to $-\boldsymbol{M}_1$ and $\boldsymbol{M}_2$ are given by

$$\begin{bmatrix} \tilde{H}_x \\ \tilde{H}_z \end{bmatrix}_{d_1^-} = -\begin{bmatrix} \tilde{G}^1_{xx} & \tilde{G}^1_{xz} \\ \tilde{G}^1_{zx} & \tilde{G}^1_{zz} \end{bmatrix} \begin{bmatrix} \tilde{M}_{1x} \\ \tilde{M}_{1z} \end{bmatrix} + \begin{bmatrix} \tilde{G}^2_{xx} & \tilde{G}^2_{xz} \\ \tilde{G}^2_{zx} & \tilde{G}^2_{zz} \end{bmatrix} \begin{bmatrix} \tilde{M}_{2x} \\ \tilde{M}_{2z} \end{bmatrix}, \qquad d = d_1 - d_2. \quad (2)$$

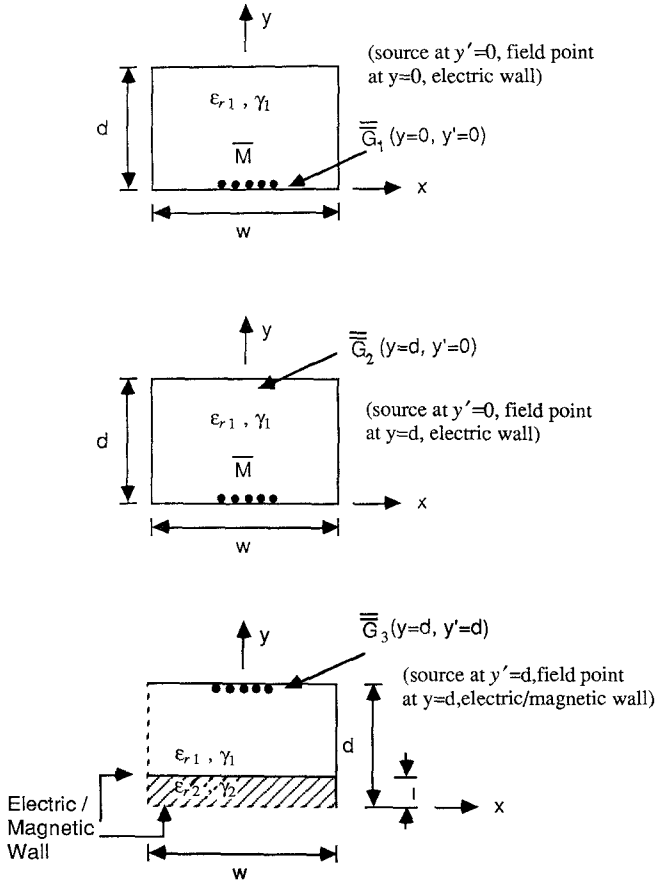

Fig 3. The three different Green's functions for field calculations.

Further, the magnetic fields at $y = d_2^+$ due to $-\boldsymbol{M}_1$ and $\boldsymbol{M}_2$ are given by

$$\begin{bmatrix} \tilde{H}_x \\ \tilde{H}_z \end{bmatrix}_{d_2^+} = -\begin{bmatrix} \tilde{G}^2_{xx} & \tilde{G}^2_{xz} \\ \tilde{G}^2_{zx} & \tilde{G}^2_{zz} \end{bmatrix}\begin{bmatrix} \tilde{M}_{1x} \\ \tilde{M}_{1z} \end{bmatrix} + \begin{bmatrix} \tilde{G}^1_{xx} & \tilde{G}^1_{xz} \\ \tilde{G}^1_{zx} & \tilde{G}^1_{zz} \end{bmatrix}\begin{bmatrix} \tilde{M}_{2x} \\ \tilde{M}_{2z} \end{bmatrix}, \quad d = d_1 - d_2. \tag{3}$$

Finally, the magnetic fields at $y = d_2^-$ due to $-\boldsymbol{M}_2$ are given by

$$\begin{bmatrix} \tilde{H}_x \\ \tilde{H}_z \end{bmatrix}_{d_2^-} = -\begin{bmatrix} \tilde{G}^3_{xx} & \tilde{G}^3_{xz} \\ \tilde{G}^3_{zx} & \tilde{G}^3_{zz} \end{bmatrix}\begin{bmatrix} \tilde{M}_{2x} \\ \tilde{M}_{2z} \end{bmatrix}, \qquad d = d_2,\ l = t. \tag{4}$$

After enforcing the continuity of the transverse magnetic field across the apertures at $y = d_1$ and d_2 in the spatial domain, one obtains

$$\begin{bmatrix} H_x \\ H_z \end{bmatrix}_{d_1^+} = \begin{bmatrix} H_x \\ H_z \end{bmatrix}_{d_1^-} \tag{5}$$

$$\begin{bmatrix} H_x \\ H_z \end{bmatrix}_{d_2^+} = \begin{bmatrix} H_x \\ H_z \end{bmatrix}_{d_2^-}. \tag{6}$$

Note that (5) and (6) are not valid in the transform domain when the different quantities are replaced by their Fourier transforms, because different transform variables exist on the two sides of the apertures.

The spectral Galerkin method is then applied by expanding the unknown magnetic surface currents $\boldsymbol{M}_1$ and $\boldsymbol{M}_2$ in (1)–(4) with sets of known basis functions weighed with unknown coefficients. To determine the unknown weighting coefficients, the transverse magnetic fields at $y = d_1$ and $y = d_2$ are tested, respectively, with the same basis functions for $\boldsymbol{M}_1$ and $\boldsymbol{M}_2$. As mentioned in [14], testing in the spatial domain for (5) and (6) corresponds to evaluating the integral $\int_{-L/2}^{L/2} w(x)h(x)\,dx$, where $w(x)$ is a basis function, $h(x)$ is a field quantity, and $L = a$ for $y = d_1^+$, b for $y = d_1^-$ and $y = d_2^+$, and c for $y = d_2^-$. Note that the integration limits are different for the two sides of (5) and (6), which is possible because the basis functions for $\boldsymbol{M}_1$ and $\boldsymbol{M}_2$ are zero outside their corresponding apertures. Applying the Parseval theorem then leads to the replacement of each integral by an inner product defined in the transform domain as the summation of $\tilde{w}\tilde{h}/L$ over a distance transform variable. Then, using (1)–(4), one obtains

$$\begin{aligned} 1/a&\begin{bmatrix} \tilde{M}_{1x}\tilde{G}^1_{xx}\tilde{M}_{1x} & \tilde{M}_{1x}\tilde{G}^1_{xz}\tilde{M}_{1z} \\ \tilde{M}_{1z}\tilde{G}^1_{zx}\tilde{M}_{1x} & \tilde{M}_{1z}\tilde{G}^1_{zz}\tilde{M}_{1z} \end{bmatrix}_{\alpha_a}\begin{bmatrix} C_{M1x} \\ C_{M1z} \end{bmatrix} \\ &= -1/b\begin{bmatrix} \tilde{M}_{1x}\tilde{G}^1_{xx}\tilde{M}_{1x} & \tilde{M}_{1x}\tilde{G}^1_{xz}\tilde{M}_{1z} \\ \tilde{M}_{1z}\tilde{G}^1_{zx}\tilde{M}_{1x} & \tilde{M}_{1z}\tilde{G}^1_{zz}\tilde{M}_{1z} \end{bmatrix}_{\alpha_b}\begin{bmatrix} C_{M1x} \\ C_{M1z} \end{bmatrix} \\ &\quad +1/b\begin{bmatrix} \tilde{M}_{1x}\tilde{G}^2_{xx}\tilde{M}_{2x} & \tilde{M}_{1x}\tilde{G}^2_{xz}\tilde{M}_{2z} \\ \tilde{M}_{1z}\tilde{G}^2_{zx}\tilde{M}_{2x} & \tilde{M}_{1z}\tilde{G}^2_{zz}\tilde{M}_{2z} \end{bmatrix}_{\alpha_b}\begin{bmatrix} C_{M2x} \\ C_{M2z} \end{bmatrix} \end{aligned} \tag{7}$$

$$\begin{aligned} &-1/b\begin{bmatrix} \tilde{M}_{2x}\tilde{G}^2_{xx}\tilde{M}_{1x} & \tilde{M}_{2x}\tilde{G}^2_{xz}\tilde{M}_{1z} \\ \tilde{M}_{2z}\tilde{G}^2_{zx}\tilde{M}_{1x} & \tilde{M}_{2z}\tilde{G}^2_{zz}\tilde{M}_{1z} \end{bmatrix}_{\alpha_b}\begin{bmatrix} C_{M1x} \\ C_{M1z} \end{bmatrix} \\ &\quad +1/b\begin{bmatrix} \tilde{M}_{2x}\tilde{G}^1_{xx}\tilde{M}_{2x} & \tilde{M}_{2x}\tilde{G}^1_{xz}\tilde{M}_{2z} \\ \tilde{M}_{2z}\tilde{G}^1_{zx}\tilde{M}_{2x} & \tilde{M}_{2z}\tilde{G}^1_{zz}\tilde{M}_{2z} \end{bmatrix}_{\alpha_b}\begin{bmatrix} C_{M2x} \\ C_{M2z} \end{bmatrix} \\ &= -1/c\begin{bmatrix} \tilde{M}_{2x}\tilde{G}^3_{xx}\tilde{M}_{2x} & \tilde{M}_{2x}\tilde{G}^3_{xz}\tilde{M}_{2z} \\ \tilde{M}_{2z}\tilde{G}^3_{zx}\tilde{M}_{2x} & \tilde{M}_{2z}\tilde{G}^3_{zz}\tilde{M}_{2z} \end{bmatrix}_{\alpha_c}\begin{bmatrix} C_{M2x} \\ C_{M2z} \end{bmatrix} \end{aligned} \tag{8}$$

where C_{M1} and C_{M2} are the weighting coefficients for $\boldsymbol{M}_1$ and $\boldsymbol{M}_2$, the $\tilde{G}$'s are the spectral Green's functions, and α_a, α_b, and α_c represent the discrete Fourier transform variables in regions with sidewall separations a, b, and c, respectively. Note that the summations over all spectral variables and basis functions are omitted in (7) and (8) for clarity. The propagation constant k_z is given by the eigenvalues of the combined matrix equations (7) and (8), which can then be solved for the unknown weighting coefficients. The fields and impedances can then be obtained. It should be noted that this method is different from the modified mode-matching technique presented in [17], although they are related and allow one to treat similar waveguide structures.

The other structures shown in Fig. 2 can be treated with a similar procedure. The equivalence principle is invoked to replace apertures by perfectly conducting planes and restore the fields with unknown magnetic surface currents

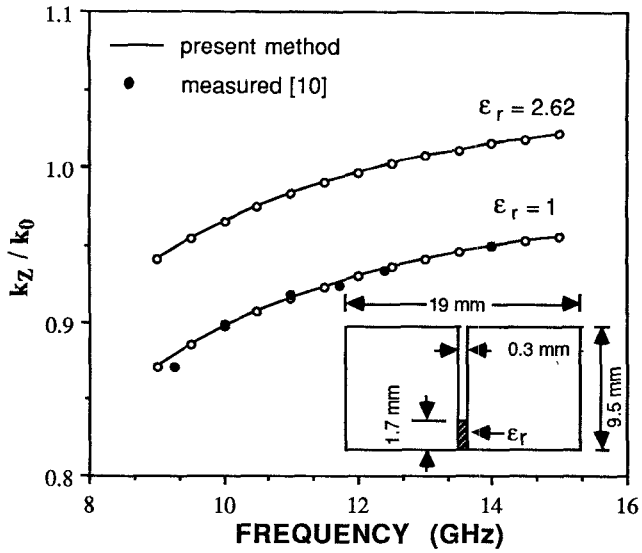

Fig. 4. Normalized propagation constant versus frequency for dielectric-loaded single-ridge waveguides.

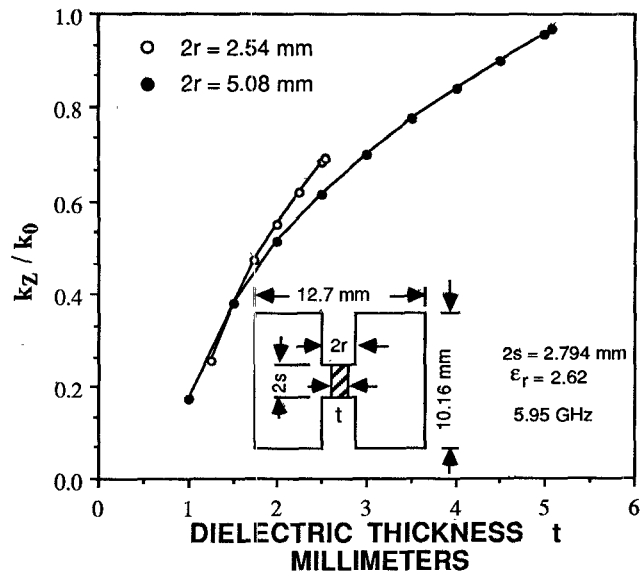

Fig. 5. Normalized propagation constant versus dielectric slab thickness for dielectric double-ridge waveguides.

located at the two sides of each aperture. Transverse magnetic fields at each aperture can then be expressed in terms of these magnetic currents and the spectral dyadic Green's functions shown in Fig. 3. Enforcing the continuity of the transverse magnetic fields at each aperture will give equations similar to (5) and (6). Then, applying the spectral Galerkin method outlined above will lead to matrix equations similar to (7) and (8).

B. Choice of Basis Functions

For the structures shown in Fig. 2(a) and (b), the basis functions provided in [18] will be used. These basis functions incorporate a singularity behavior of $x^{-1/2}$ at both edges of an aperture for the z-components of the magnetic currents. As discussed in [14], they are adequate for approximating the currents on an aperture with two edges. As for the antipodal ridge waveguide structure shown in Fig. 2(c), the aperture current only has singularity behavior for M_z at one of the edges, namely, the edge of the ridge. Further, M_x is zero at the original waveguide sidewalls. Hence, new types of current basis functions need to be used. For the apertures located at $-d_3$ and $-d_4$, the basis functions for M_x and M_z are respectively given by

$$\zeta_i(x) = \sin(k_i x)/\sqrt{b^2 - x^2}, \qquad k_i = i\pi/b, \quad i = 1,2,\cdots \tag{9}$$

$$\eta_i(x) = \cos(k_i x)/\sqrt{b^2 - x^2}, \qquad k_i = i\pi/b, \quad i = 0,1,2,\cdots. \tag{10}$$

For the apertures located at d_1 and d_2, the basis functions for M_x and M_z are similar to those given in (9) and (10), but with x replaced by $(x-h)$ in the numerator and $(x-a)$ in the denominator, and $h = (a-b)$. The Fourier transforms of these basis functions were found to be complicated functions of zero-order Bessel functions of the first kind and zero-order Struve functions. As for the T-septum waveguide, basis functions similar to those specified in (9) and (10) are used. Lastly it should be noted that sine and cosine transforms need to be used appropriately to satisfy the boundary conditions for the antipodal and T-septum waveguides.

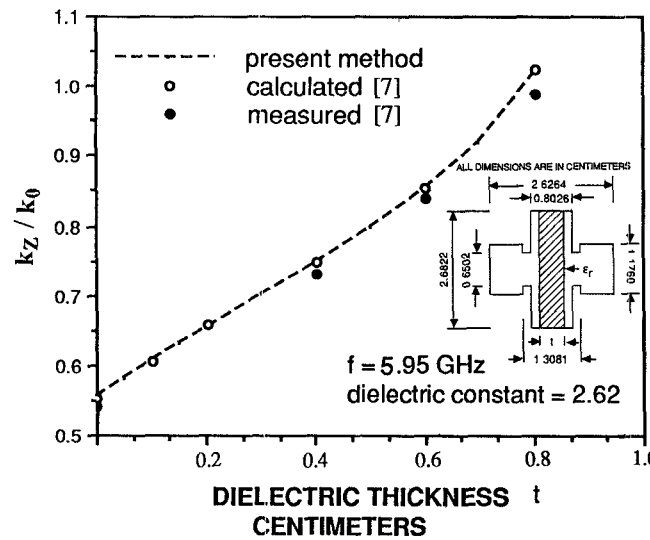

Fig. 6. Normalized propagation constant versus dielectric slab thickness for a slotted dielectric-loaded ridge waveguide.

III. Results

As an illustration of the versatility and validity of the method, numerical results on the normalized propagation constant for the dominant mode are obtained in Figs. 4–7, respectively, for a single-ridge waveguide, a double-ridge waveguide, a slotted ridge waveguide, and an antipodal ridge waveguide, all being dielectric-loaded. Three basis functions for each component of the magnetic surface current are used. The Fourier transform variables are $\alpha_a = n\pi/a$, $\alpha_b = n\pi/b$, and $\alpha_c = n\pi/c$ for the regions with sidewall separations a, b, and c in Fig. 2. As one can see in all the results, the propagation characteristic can be

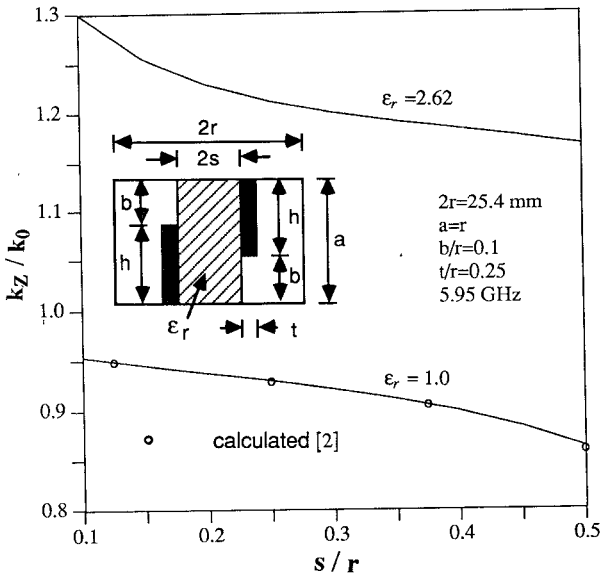

Fig. 7. Normalized propagation constant versus ridge spacing for dielectric-loaded antipodal ridge waveguides.

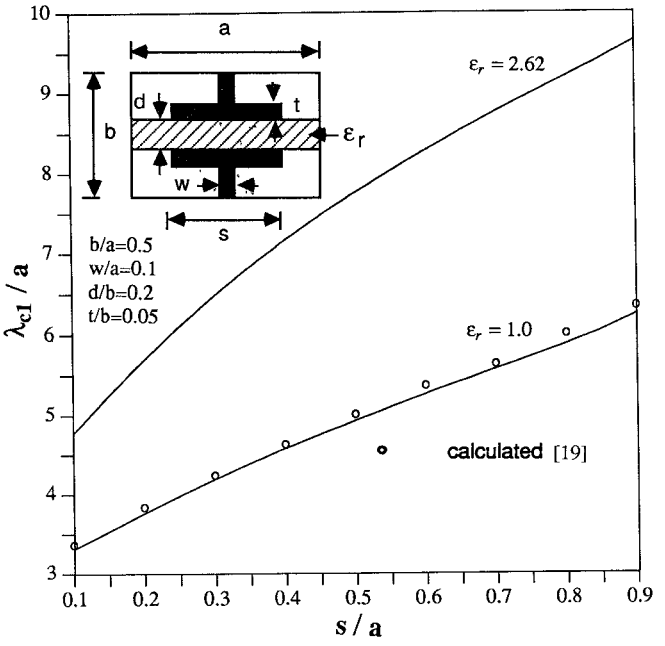

Fig. 8. Cutoff wavelength normalized to the sidewall separation a versus sidewall separation for the first TE mode for dielectric-loaded T-septum waveguides

greatly affected by dielectric loading. As shown in Fig. 4, the frequency dependence of k_z is about the same for the two dielectric slabs considered ($\epsilon_r = 1.0$ and 2.62). Also, in Fig. 5, one can observe the cutoff effect, as k_z approaches zero, due to a decrease in cutoff wavelength when the dielectric slab thickness t is decreased. Such a decrease in cutoff wavelength can also be seen in Fig. 6 when the dielectric slab thickness is decreased. In addition, the results for the antipodal ridge waveguide in Fig. 7 demonstrate a fairly large dependence on the dielectric constant of the slab. Such a dependence can also be seen in the results shown in Fig. 8 on the normalized cutoff wavelength for the first TE mode for a T-septum waveguide. In this case, $\alpha_a = n\pi/a$, $\alpha_b = n\pi/b$, and $\alpha_c = (n+1/2)\pi/c$. If an electric wall is placed at $x = 0$, then α_c should be changed to $n\pi/c$. In all cases, comparisons with previous numerical and experimental results are excellent.

IV. Conclusions

A simple and numerically efficient mixed spectral-domain method has been presented for the analysis of generalized dielectric-loaded ridge waveguides. The formulation allows one to maintain the advantages of the spectral-domain immittance approach in more complicated structures, which requires mixing two different spectral domains on the two sides of an aperture. Due to the nature of the approach, dielectric slabs can be incorporated easily. Representative results for different structures compare well with those obtained previously with different methods.

Appendix

The spectral dyadic Green's functions shown in Fig. 3 are given by

$$\begin{bmatrix} \tilde{G}^1_{xx} & \tilde{G}^1_{xz} \\ \tilde{G}^1_{zx} & \tilde{G}^1_{zz} \end{bmatrix} = -\begin{bmatrix} Y^{1h}N_x^2 + Y^{1e}N_z^2 & (Y^{1h}-Y^{1e})N_xN_z \\ (Y^{1h}-Y^{1e})N_xN_z & Y^{1h}N_z^2 + Y^{1e}N_x^2 \end{bmatrix} \tag{A1}$$

$$\begin{bmatrix} \tilde{G}^2_{xx} & \tilde{G}^2_{xz} \\ \tilde{G}^2_{zx} & \tilde{G}^2_{zz} \end{bmatrix} = -\begin{bmatrix} Y^{2h}N_x^2 + Y^{2e}N_z^2 & (Y^{2h}-Y^{2e})N_xN_z \\ (Y^{2h}-Y^{2e})N_xN_z & Y^{2h}N_z^2 + Y^{2e}N_x^2 \end{bmatrix} \tag{A2}$$

$$\begin{bmatrix} \tilde{G}^3_{xx} & \tilde{G}^3_{xz} \\ \tilde{G}^3_{zx} & \tilde{G}^3_{zz} \end{bmatrix} = -\begin{bmatrix} Y^{3h}N_x^2 + Y^{3e}N_z^2 & (Y^{3h}-Y^{3e})N_xN_z \\ (Y^{3h}-Y^{3e})N_xN_z & Y^{3h}N_z^2 + Y^{3e}N_x^2 \end{bmatrix} \tag{A3}$$

$$Y^{1e,h} = Y_1^{\mathrm{TM,TE}}\coth(\gamma_1 d) \tag{A4}$$

$$Y^{2e,h} = Y_1^{\mathrm{TM,TE}}/\sinh(\gamma_1 d) \tag{A5}$$

$$Y^{3e,h} = Y_1^{\mathrm{TM,TE}}\frac{Y_1^{\mathrm{TM,TE}} + Y_2^{\mathrm{TM,TE}}\coth[\gamma_1(d-l)]Q}{Y_1^{\mathrm{TM,TE}}\coth[\gamma_1(d-l)] + Y_2^{\mathrm{TM,TE}}Q}. \tag{A6}$$

Here $Q = \coth(\gamma_2 l)$ and $\tanh(\gamma_2 l)$ for an electric and a magnetic wall placed at $x = 0$ respectively. In addition,

$$Y_i^{\mathrm{TE}} = -\frac{\gamma_i}{j\omega\mu_0} \tag{A7}$$

$$Y_i^{\mathrm{TM}} = \frac{-j\omega\epsilon_{ri}\epsilon_0}{\gamma_i} \tag{A8}$$

$$\gamma_i = \left(\alpha^2 + k_z^2 - \epsilon_{ri}k_0^2\right)^{1/2} \tag{A9}$$

$$N_x = \frac{\alpha}{\sqrt{\alpha^2 + k_z^2}} \tag{A10}$$

$$N_z = \frac{k_z}{\sqrt{\alpha^2 + k_z^2}} \tag{A11}$$

where α is the Fourier transform variable and $k_z(\beta)$ is the propagation constant in the z direction.

REFERENCES

[1] S. Hopfer, "The design of ridged waveguides," *IRE Trans. Microwave Theory Tech.*, vol. MTT-3, pp. 20–29, Oct. 1955.

[2] D. Dasgupta and P. K. Saha, "Rectangular waveguide with two double ridges," *IEEE Trans. Microwave Theory Tech.*, vol. MTT-31, pp. 938–941, Nov. 1983.

[3] G. G. Mazumder and P. K. Saha, "A novel rectangular waveguide with double T-septums," *IEEE Trans. Microwave Theory Tech.*, vol. MTT-33, pp. 1235–1238, Nov. 1985.

[4] Y. Konishi, K. Uenakada, N. Yazawa, N. Hoshino, and T. Takahashi, "Simplified 12-GHz low-noise converter with mounted planar circuit in waveguide," *IEEE Trans. Microwave Theory Tech.*, vol. MTT-22, pp. 451–454, Apr. 1974.

[5] L.-P. Schmidt and H. Meinel, "Broadband millimeter-wave PIN-diode attenuator with double-ridged waveguide flanges," *Electron. Lett.*, vol. 18, no. 19, pp. 839–840, Sep. 1982.

[6] J. Bornemann and F. Arndt, "Modal *S*-matrix design of optimum stepped ridged and finned waveguide transformers," *IEEE Trans. Microwave Theory Tech.*, vol. MTT-35, pp. 561–567, June 1987.

[7] A. T. Villeneuve, "Analysis of slotted, dielectrically loaded, ridged waveguide," *IEEE Trans. Microwave Theory Tech.*, vol. MTT-32, pp. 1302–1310, Oct. 1984.

[8] T. S. Chen, "Calculations of the parameters of ridge waveguides," *IRE Trans. Microwave Theory Tech.*, vol. MTT-5, pp. 12–17, Jan. 1957.

[9] J. P. Montgomery, "On the complete eigenvalue solution of ridged waveguide," *IEEE Trans. Microwave Theory Tech.*, vol. MTT-19, pp. 547–555, June 1971.

[10] Y. Utsumi, "Variational analysis of ridged waveguide modes," *IEEE Trans. Microwave Theory Tech.*, vol. MTT-33, pp. 111–120, Feb. 1985.

[11] G. G. Mazumder and P. K. Saha, "Rectangular waveguide with T-shaped septa," *IEEE Trans. Microwave Theory Tech.*, vol. MTT-35, pp. 201–204, Feb. 1987.

[12] P. K. Saha and G. G. Mazumder, "Bandwidth characteristics of inhomogeneous T-septum waveguides," *IEEE Trans. Microwave Theory Tech.*, vol. 37, pp. 1021–1026, June 1989.

[13] T. Itoh, "Spectral domain immittance approach for dispersion characteristics of generalized printed transmission lines," *IEEE Trans. Microwave Theory Tech.*, vol. MTT-28, pp. 733–736, July 1980.

[14] C. H. Chan, K. T. Ng, and A. B. Kouki, "A mixed spectral domain approach for dispersion analysis of suspended planar transmission lines with pedestals," *IEEE Trans. Microwave Theory Tech.*, vol. 37, Nov. 1989.

[15] R. F. Harrington, *Time-Harmonic Electromagnetic Fields*. New York: McGraw-Hill, 1961.

[16] T. Itoh and R. Mittra, "A technique for computing dispersion characteristics of shielded microstrip lines," *IEEE Trans. Microwave Theory Tech.*, vol. MTT-22, pp. 896–898, Oct. 1974.

[17] R. Vahldieck and J. Bornemann, "A modified mode-matching technique and its application to a class of quasi-planar transmission lines," *IEEE Trans. Microwave Theory Tech.*, vol. MTT-33, pp. 916–926, Oct. 1985.

[18] E. G. Farr, C. H. Chan, and R. Mittra, "A frequency-dependent coupled-mode analysis of multiconductor microstrip lines with application to VLSI interconnection problems," *IEEE Trans. Microwave Theory Tech.*, vol. MTT-34, pp. 307–310, Feb. 1986.

[19] F. J. German and L. S. Riggs, "Bandwidth properties of rectangular T-septum waveguides," *IEEE Trans. Microwave Theory Tech.*, vol. 37, pp. 917–919, May 1989.

Kwong T. Ng (S'78–M'79) received the B.Eng. (Hons.) degree from McGill University, Montreal, Quebec, Canada, in 1979, and the M.S. and Ph.D. degrees from Ohio State University, Columbus, in 1981 and 1985, respectively, all in electrical engineering.

From 1979 to 1984, he was with the ElectroScience Laboratory at Ohio State University, where he worked on numerical electromagnetics, phased arrays, frequency-selective surfaces, and radomes. Since 1985, he has been with the University of Virginia, Charlottesville, where he is currently an Assistant Professor of Electrical Engineering. His current research interests include numerical electromagnetics, phased arrays, frequency-selective surfaces, and millimeter-wave components.

Chi Hou Chan (S'86–M'86) attended Hong Kong Polytechnic and the City College of New York. He received the B.S. and M.S. degrees in electrical engineering from Ohio State University, Columbus, in 1981, and 1982, respectively, and the Ph.D. degree in electrical engineering from the University of Illinois, Urbana, in 1987.

From 1981 to 1982, he was a Graduate Research Associate at the ElectroScience Laboratory, Ohio State University. From 1987 to 1989, he was a Visiting Assistant Professor with the Electromagnetic Communication Laboratory in the Department of Electrical and Computer Engineering at the University of Illinois. In September 1989, he joined the University of Washington, Seattle, as an Assistant Professor. His research interests include numerical techniques in electromagnetics, frequency-selective surfaces, microwave integrated circuits, high-speed digital circuits, and wave propagation in anisotropic medium for integrated optics applications.

Dr. Chan is an associate member of URSI Commission B.